Research Square

Preprints are preliminary reports that have not undergone peer review.
They should not be considered conclusive, used to inform clinical practice,
or referenced by the media as validated information.

Transitional calcite-aragonite stacking as a signature of hexagonal aragonite in biogenic and inorganic deposits

Péter Nèmeth

nemeth.peter@csfk.org

HUN-REN Research Centre for Astronomy and Earth Sciences https://orcid.org/0000-0001-5592-5877

Mihály Pósfai

University of Pannonia

Attila Demény

Research Centre for Astronomy and Earth Sciences

Peter Pekker

University of Pannonia

Aleksander Recnik

Jozef Stefan Institute https://orcid.org/0000-0002-6636-8591

Vesna Ribić

Jozef Stefan Institute https://orcid.org/0000-0001-8185-7433

Pavel Gavryushkin

V.S. Sobolev Institute of Geology and Mineralogy, Russian Academy of Science, Siberian Branch
https://orcid.org/0000-0002-9419-2167

Maksim Banaev

V.S. Sobolev Institute of Geology and Mineralogy, Siberian Branch of Russian Academy of Sciences

Marco Bruno

University of Turin

Christoph Spötl

University of Innsbruck https://orcid.org/0000-0001-7167-4940

Michael Pettauer

Institute of Applied Geosciences, NAWI Graz Geocenter, Graz University of Technology
https://orcid.org/0000-0003-4383-3945

Martin Dietzel

Graz University of Technology https://orcid.org/0000-0003-2222-2459

Levente Illes

Centre for Energy Research

Article

Keywords:

Posted Date: June 4th, 2026

DOI: https://doi.org/10.21203/rs.3.rs-9567838/v1

License: This work is licensed under a Creative Commons Attribution 4.0 International License.
Read Full License

Additional Declarations: There is **NO** Competing Interest.

Abstract

Aragonite abundantly crystallizes in marine and continental environments and occurs ubiquitously in biominerals, despite being metastable under ambient conditions. To resolve this apparent contradiction, we studied the crystal structure of aragonite that grew on calcite of biogenic (Berger Károly cave; Hungary) and inorganic (Sonnenberg; Italy and Erzberg; Austria) origin, in a range of natural settings and temperatures. Electron microscopy measurements show (001) stacking faults (SFs) in the first-grown aragonite. Structural modelling combined with theory-based optimization suggests that the crystal structure of this new type of SF can be explained by the presence of (000l) calcite-like layers within aragonite. Abundant (0001) calcite twins occur in the last-grown calcite, and hexarag, the hypothetical hexagonal polymorph of aragonite, was identified across the calcite twin interfaces. Oxygen isotope data indicate that both the Berger-Károly and Sonnenberg samples formed under non-equilibrium conditions, whereas the Erzberg aragonite formed near equilibrium, possibly explaining the defect-free structure. The presence of (001) SFs and (0001) calcite twins testifies to the formation of transitional calcite-aragonite structures, suggests the occurrence of a hexarag precursor phase and provides new insights into the long-debated mechanism of metastable aragonite formation in dynamically evolving (bio)geologic environments.

Introduction

Aragonite is a calcium carbonate polymorph that is metastable at Earth's near-surface conditions, yet it is widespread in marine and, less commonly, in terrestrial environments[1–4]. Aragonite commonly occurs in caves[5–6], hot springs[7], hydrothermal veins[8–9], as well as in iron ore deposits[10]. It is also an important biomineral and serves as a major skeletal and framework-building component of mollusks, corals and stromatolites[11–13]. Aragonite precipitated on calcite occurs in many types of sediments and sedimentary rocks, but the mechanisms behind this phenomenon remain poorly understood[2, 14–15].

The formation of metastable aragonite is attributed to various abiotic and biotic factors, including an elevated molar Mg^{2+}/Ca^{2+} ratio of the aqueous solution (> 2)[16–18] and pH > 8.2 [19]. Mavromatis et al.[20] demonstrated that the Mg partition coefficient between aragonite and the fluid is controlled by growth rate and temperature. At constant growth rates, Mg incorporation decreases as temperature increases from 5 to 25°C. At molar ratios of Mg^{2+}/Ca^{2+} > 2.0 in the fluid, the surface energy of aragonite is lower than that of Mg-bearing calcite, promoting aragonite precipitation[21]. On the other hand, organic macromolecules can modify the local physico-chemical microenvironment, thereby providing favorable conditions for the formation of aragonite instead of (Mg)calcite[22–23]. Nahi et al. [24] demonstrated that polyamines also promote aragonite nucleation and suggested that organisms could control polymorph selection by exploiting amine-rich organic molecules.

Various precursor phases have been invoked to explain aragonite formation. In particular, a specific type of amorphous calcium carbonate (ACC), called protoaragonite (pAra), was observed in biogenic

carbonates[25–26], as well as in laboratory experiments[27–29]. Walker et al.[29] demonstrated the attachment of ACC nanoparticles and their transformation into aragonite mesocrystals by visualizing the early stages of the crystallization process via cryo transmission electron microscopy (TEM). Applying scanning TEM (STEM), Molnár et al.[30] reported the formation of spindle-shaped aragonite from Mg-bearing ACC under a range of dissolved Mg^{2+} concentrations, and suggested that aragonite crystallization occurred via partial dissolution and re-precipitation. Radha et al.[31] emphasized that during aragonite formation may involve a series of ordering, dehydration, and crystallization processes, which progressively lower the free energy of the system.

Aragonite formation from crystalline precursors was also reported, in particular in aqueous solutions. Ogino et al.[32] showed that vaterite first crystallizes to aragonite and then to calcite via dissolution/re-precipitation processes. Aragonite crystallization from monohydrocalcite ($CaCO_3xH_2O$)[33] and calcium carbonate hemihydrate ($CaCO_3x1/2H_2O$)[34], both of which were prepared from Mg-containing solutions, was also demonstrated. Lázár et al.[36] found that ikaite ($CaCO_3x6H_2O$) can transform into aragonite if the parent solution contains some Mg^{2+} (26 mg/l). In all these cases, aragonite formation occurred via dissolution of the metastable anhydrous or hydrous phase.

Other $CaCO_3$ polymorphs were also proposed as precursors of aragonite. In particular, Németh et al.[36] demonstrated the precipitation of a nanocrystalline monoclinic aragonite (mAra) form in a cave. They showed that mAra is crystallographically related to aragonite and exhibits a layered structure in which some carbonate ions are replaced by hydroxyl groups, with up to 10 atomic % Mg incorporated. Gavryushkin et al.[37] showed that the atomic arrangement of the {110} multiply twinned aragonite, referred as tAra, is an intermediate between aragonite and amorphous pAra and suggested that tAra as a precursor of aragonite. A molecular dynamics study, performed at high temperature (~323°C), suggested that aragonite transforms to calcite via hexarag, the hexagonal polymorph of aragonite (38). Using theoretical calculations, Bruno et al.[39] demonstrated the presence of hexarag at both epitaxial and relaxed (001)aragonite/(0001)calcite interfaces, and proposed that this polymorph plays a role in the transformation of aragonite to calcite under ambient conditions. They hypothesized that hexarag occurs at the nanoscale in intimate structural association with both calcite and aragonite; however, its existence has not yet been experimentally confirmed.

Here, we investigate samples of aragonite grown on biogenic and inorganic calcite substrate in order to gain insights into the formation of metastable aragonite. This process has traditionally been studied using samples synthesized from artificial $Na(HCO_3)$, $MgCl_2$ and $CaCl_2$ solutions, which are uncommon in natural environments. We selected samples from Berger Károly cave (Tapolca, Hungary), Sonnenberg (Italy) and Erzberg (Austria), formed in distinct geologic environments, to examine their nanostructure and geochemistry. High-resolution (HR) high-angle annular dark-field (HAADF) STEM images and density functional theory (DFT) calculations reveal a new type of defect that we attribute to the incorporation of (0001) calcite layers within the aragonite structure and the occurrence of a hexarag precursor phase. We

propose that the findings can be generalized and that the observed defects are relevant for understanding metastable aragonite formation in biogenic and inorganic deposits.

Results

Samples and the aragonite-calcite interface

The calcite-aragonite interface was studied in (1) ~20,000-year-old samples that formed at ~25 °C in an underground lake in the Berger Károly cave in Tapolca[14], (2) ~14,000-year-old specimens that formed at 12 °C in fractures of the Sonnenberg (Italy)[40], and (3) modern (5-year-old) deposits from the Erzberg (Austria), which formed at 5 °C[15] (Fig. S1). Samples were carefully selected to allow identification of the growth directions as well as the last-formed calcite and the first-grown aragonite, i.e., the interface between calcite and aragonite (Figure 1).

Transmitted-light microscope images of thin sections revealed sharp boundaries between aragonite and calcite in all samples (Figs. 1A, D, G). Both the Berger Károly cave and the Sonnenberg samples are characterized by layered growth of needle-shaped aragonite crystals on calcite. In contrast, the Erzberg specimen shows aragonite needles growing radially on the calcite core (Fig. 1G). The Berger Károly cave sample is unique in that aragonite crystals grew on the top of botryoidal calcite[14] (Fig. S2a). The underlying calcite has a stromatolitic fabric, and its uppermost microlayer displays textural features characteristic of algal mats, including folding and tearing. The contact between the calcite substrate and the overlying aragonite crystals resembles bacterial forms (cf. [41-42]). These features suggest that both the stromatolite-like calcite deposit and the terminal microlayer represent microbially mediated calcite formation. This calcite layer is porous and also contains clay minerals (Fig. S2b). Compared to the Berger Károly cave sample, smaller (5-20 µm-sized) elongated aragonite crystals are present in both the Sonnenberg and Erzberg samples.

Back-scattered electron (BSE) images (Fig. 1B, E, H) combined with energy dispersive X-ray (EDX) analysis indicate that the last-formed calcite contains some Mg (~4% $MgCO_3$), whereas the Mg content of the first-formed aragonite is always low (< 1.5 % $MgCO_3$) (Fig. 1C, F, I). The Mg content slightly increases toward the calcite-aragonite boundary, in agreement with the observations of Eichinger et al.[15]. To investigate the crystal structure of the interfaces of calcite and aragonite, ~2–3 µm-wide TEM lamellae were prepared using focused ion beam (FIB) thinning across the boundary between the last- and first-formed carbonates.

Stable carbon and oxygen isotope compositions of the aragonite and calcite samples from the three locations are listed in Table S1. There is a distinct difference between the aragonite and the calcite of the Berger Károly Cave's sample (L-top) with the aragonite enriched in ^{18}O and ^{12}C relative to the adjacent calcite. The Sonnenberg sample (LAS34b) yielded different carbon and oxygen isotope data distributions with the aragonite significantly enriched in both ^{13}C and ^{18}O relative to the calcite (Fig. 1J). The Erzberg sample contained only aragonite, whose $\delta^{13}C$ value is transitional between the L-top and LAS34b

compositions. The $\delta^{18}O$ values reflect the differences in formation temperatures and water compositions[43] at the studied locations (see Materials and Methods section). The aragonite-water oxygen isotope fractionations were calculated using these data (Fig. 1K).

A new type of aragonite stacking faults (SFs) in first-grown aragonite

The first-grown aragonite of the Berger Károly cave sample consists of 1 µm long and ~200 nm wide slabs (inset, Fig. 2A, Figs. S3, S4), which are elongated along [001]. Bright-field TEM (BFTEM) images of the calcite-aragonite transition band, recorded in [100] projection of aragonite, display a high density of basal-plane faults that produce a lamellar, mottled texture with 5-20 nm-sized subdomains.

Similarly, (001) SFs also occur in the Sonnenberg sample. Their presence is confirmed by BFTEM and HRTEM images, as well as by selected area electron-diffraction (SAED) patterns and FFTs (Figs. 2C, E, S5). The relatively thick TEM1 region in which these defects occur did not allow imaging at higher resolution. In this region, SFs are less abundant and partition the grains into larger domains (20-40 nm) (Fig. S5) compared to the Berger Károly cave sample. In contrast, we found no evidence for the occurrence of (001) SFs in the Erzberg sample (Figs. 2D, F, S6). The TEM investigation of this sample yielded a sharp interface between aragonite and calcite (Fig. 2G). The aragonite crystals are relatively homogeneous, and neither the mottled texture nor the streaked reflections are present (Fig. S6).

SAED patterns acquired from defect areas show a distinct streaking of reflections parallel to c* (<001>) (Figs. 2B, E), indicating the presence of numerous planar defects oriented parallel to the basal planes of aragonite. Because these defects arise from disruptions in the regular stacking of (001) aragonite atomic planes, we refer to them as (001) SFs. These features are present not only along the [100] projection, but in all projections along the <*hk*0> prism band that provide an edge-on view of the basal planes. An example recorded along the [110] direction of aragonite in the Berger Károly cave sample is shown in Fig. S4. To our knowledge, similar defects have not been previously reported in aragonite.

In [100] projection, a pseudohexagonal close-packed (*p-hcp*) stacking of the Ca-layers along the crystallographic *c*-axis is resolved as a zig-zag pattern, which is clearly seen in high-resolution HAADF STEM images (Fig. 3). Any disruption of this p-hcp stacking represents a stacking fault, expressed as a planar defect in real space or as streaking parallel to *c** in reciprocal space. Figure 3A shows a small segment of the calcite-aragonite transition zone containing multiple SFs. Owing to strain and thickness effects, not all defects are equally well resolved; nevertheless, each reflects some form of stacking disorder along the c axis. The simplest variant, characterized by a regular stacking sequence and distinct contrast, is outlined in Fig. 3A and shown at higher resolution in Fig 3C. It is interesting that the 10-20 nm-long straight segments of the SFs are connected by lateral sidesteps.

The intensity maxima in HAADF-STEM images roughly corresponds to atomic columns. Such Z-contrast images can therefore be used to directly interpret local structures. In the case of our specimens, such an interpretation is complicated by the relatively large specimen thickness and the strain fields generated by multiple defects. Nevertheless, owing to the high density of SFs, localized regions suitable for structural

analysis could be identified. The HAADF-STEM image in Fig. 4A shows well-resolved white dots that correspond to the positions of Ca atomic columns. In ordered domains, the *p-hcp* stacking of the Ca-sublattice in [100] projection is clearly resolved. Across the SF, the contrast is blurred and does not permit further identification of atomic column positions. Instead, we used bulk translation to deduce the stacking across the interface. Close inspection suggests an ~ 1/6*b*+0.5*c* shift of the aragonite unit cell across the (001) SF (Fig. 4E). Structurally, such a shift can be reproduced by one pseudocubic close-packed (*p-ccp*) layer emplaced within the *p-hcp* sequence of aragonite. The local *p-ccp* stacking corresponds to one slab of calcite-like structure within aragonite and is similar to SFs in other close-packed structure pairs, such as wurtzite-sphalerite[44].

Curiously, FFTs of some nm-sized regions (e.g., Fig. 4D) with ordered stacking of the (001) aragonite planes show systematic absences for $k = 2n+1$ on (0*kl*), and can be indexed on the basis of a unit cell similar to that of hexarag (a= 0.496 nm, c= 0.578, $P6_322$). The d_{002} spacings of aragonite (0.287 nm) closely match that of hexarag (0.284 nm); however, the measured d_{020} spacing (0.40 nm) is smaller than the d100 spacing of hexarag (0.432 nm), and systematic absences are expected for $k = 2n+1$ on the [0*k*0] axis only. So, most likely, these hexarag-alike regions correspond to the overlapping aragonite domains associated with inclined SF steps.

(0001) calcite twins in the last-grown calcite

We studied the structure of the last-grown calcite in all specimens. The calcite crystal size of the Berger Károly cave sample (Fig. S2B) is smaller (50-500 nm) than that of the relatively large, micron-sized crystals in the Erzberg specimen (Fig. 2D, E), which can probably be explained by the biogenic versus inorganic origin.

Interestingly, the Sonnenberg sample is distinguished by mottled contrast features in the last-grown calcite (Fig. S7). The TEM image of calcite projected along [010] shows fringes with a spacing of 0.852 nm, corresponding to three times the d_{006} spacings (3x0.284 nm), within a ~20x20 nm region (Fig. 5A). In comparison to single-crystal calcite (Fig. 5C), additional reflections appear in the corresponding FFT (Fig. 5D). STEM images and FFTs calculated from selected regions demonstrate that the unusual d-spacings and the extra reflections arise from the ~10 nm-sized (0001) twinned calcite domains (Figs. 5B, E, F).

Structure models of (001) aragonite SF

(001) SFs found in the Berger Károly and the Sonnenberg specimens, and (0001) calcite twins in the Sonnenberg specimens suggest a similar structural transition process at the calcite-aragonite boundary. Whereas (0001) twins of calcite have been previously described[e.g., 45], (001) aragonite SFs are a new type of defect that has not yet been documented in the literature.

Both aragonite and calcite structures can be considered as consisting of close-packed layers of Ca atoms interweaved with CO_3 groups. Ca close-packed layers in aragonite form a pseudohexagonal ABAB

(*p-hcp*) stacking, whereas in calcite these layers are stacked in a pseudocubic ABCABC (*p-ccp*) sequence (Fig. 6). The successive Ca layers are shifted by 2/6y and 1/6y fractional coordinates in aragonite and calcite doubled along its b axis, respectively. In hexarag the Ca layers have ABAB (*p-hcp*) stacking, similar to aragonite, whereas the CO_3 groups are arranged identical to those in calcite (Fig. 6).

Interestingly, the structure across the (0001) calcite twin interface is consistent with hexarag (Fig. 6).

A SF in aragonite can be explained by shifting a successive Ca layer in aragonite by the y fractional coordinates of 1/6 (instead of 2/6). As a result, a local, calcite-type (*p-ccp*) Ca stacking sequence is produced within aragonite (Fig. 6). Similarly, a basal twin in calcite is produced by the departure of stacking from the regular p-ccp to p-hcp. In other words, observing only the Ca-sublattices, a basal-plane SF in aragonite has a calcite local structure, whereas the basal twin of calcite has a local structure of aragonite. The placement of CO_3 groups in these local structural transformations is not known. Within these deviations from regular stacking, the CO_3 groups could be either tilted from the plane perpendicular to z or have fractional coordinates resembling aragonite- or calcite-type arrangements. Their actual settings depend on local interatomic forces and can be studied by DFT calculation. To study the interface structures, various models were built (Fig. S8) based on crystal chemistry principles, taking into account local charge balance and the regular stacking and bond distances in the studied carbonate structures.

The high-resolution HAADF-STEM image of the (001) basal-plane SF in aragonite shown in Fig. 4 shows periodic contrast features in both parts on opposite sides of the SF, whereas the interface itself is diffuse, and it is hard to discern the exact positions of Ca columns. Across the SF, a lattice translation of ~1/6b+1/2c can be roughly identified by matching the Ca sublattice in the two parts of aragonite (Fig. 4E). Based on structural consideration, 3-layer *p-ccp* sequence in aragonite can be obtained by either the 180° in-plane rotation of the adjacent domains around the (001) normal at any Ca-lattice site, or the removal of a close-packed layer, followed by translation for the adjacent aragonite block. The first consideration results in oppositely oriented CO_3 groups in the translated domain compared to those in the primary domain, whereas following the second approach, the orientation of the CO_3 groups in the translated domain remains the same as it was in the primary domain. Besides bulk translations, several configurations are possible for arranging the positions of the CO_3 groups within the *p-ccp* slab: they may retain the arrangement found in the primary domain, adopt that of the secondary domain, or that of calcite. The SF models taken into consideration in our study have the following properties:

- V04 model (intrinsic SF): removal of one close-packed layer followed by translation for the adjacent aragonite block to generate a basic 3-layer *p-ccp* sequence. The CO_3 groups within the *p-ccp* slab are symmetrized to resemble those in calcite.

- V05.1 model (rotational SF): 180° in-plane rotation of the adjacent domain around the *c* normal at any Ca-lattice site, CO3 groups symmetrized in the first *ccp* layer.

- V05.2 model (rotational SF): 180° in-plane rotation of the adjacent domain around the c normal at any Ca-lattice site, CO_3 groups symmetrized in the middle *ccp* layer.

- V06 model (extrinsic SF): insertion of a calcite slab and a necessary in-plane translation for lattice continuation of the adjacent aragonite domain. The CO_3 groups within the *p-ccp* slab are not symmetric.

According to these crystallographic operations, rigid three-layer models were built (Fig. S8) and optimized by DFT calculations. The DFT relaxed models are shown in Fig. 6. The striking difference among the SF models is the cell shift of either 1/6*b*+ 1/2*c* (V05.1 and V05.2) or 4/6*b* + 1/2*c* (V04, V06) with respect to aragonite (Fig. 6). Furthermore, there are Ca coordination differences among the SF models. V04 contains exclusively 9-fold coordinated Ca, corresponding to aragonite-type coordination. In contrast, V06 includes 6-fold coordinated Ca, analogous to that in calcite, and both V05.1 and V05.2 comprise 7- and 8-fold coordinated Ca in addition to 9-fold coordinated Ca (Fig. S9). In addition, in V05.1 and V05.2 the CO3 groups adjacent to the defect layer are markedly tilted out of the horizontal plane (Fig. 7).

The DFT calculated enthalpies of reference aragonite, calcite, and hexarag are consistent with extensive available data[38], confirming that calcite is the energetically most favorable polymorph, while hexarag and aragonite show higher energies by 0.08 and 0.15 eV/f.u., respectively (Table 1). The newly identified SF structures are energetically less favorable than pure aragonite, with energy differences ranging from 0.04 to 0.164 eV/f.u. Among them, V05.1 structure is the most favorable, with an energy higher than aragonite by only 0.04 eV/f.u., followed closely by the V04 structure with a slightly higher energy, whereas V06 and V05.2 structure have higher total energies by 0.08 and 0.16 eV/f.u., respectively. Given the observed formation of aragonite following calcite crystallization, the emergence of the proposed defect structures may also be considered as a plausible transition mechanism between the two polymorphs during the crystallization process.

The defect structures show a slight deviation from the initial orthogonality of the unit cell after energy optimization. To check their stability, we performed molecular dynamic simulation of the v05.1 structure at 350 K. All units exhibit only moderate oscillations around their equilibrium positions, with no signs of structural rearrangement. This result confirms the stability of the structure and its potential occurrence under specific natural and/or experimental conditions.

The two models, V04 and V05.1, that showed the lowest total energies according to DFT calculations were further considered in our analysis of basal-plane SF in aragonite (Fig. 7). Experimental HAADF-STEM image from a short SF section shown in Fig. 4E was processed to enhance existing contrast features and remove any scanning distortions following the IMAGE-WARP procedure (described by [46]), which is based on polynomial correction of distortions using a structure-based reference grid. In our case, we used a Ca-sublattice with a 3-layer *p-ccp* SF, whereas the CO_3 groups remained free to move with Ca. Thus, the processed experimental image was compared with simulated HAADF-STEM images (Fig. 7). As expected, both models accurately reproduce the Ca sublattice, represented by strong white

dots, exhibiting a 3-layer *p-ccp* sequence across the SF. In the lower domain, both models also reproduce the positions of the weak dots arising from the CO_3 groups. In the upper domain, translated by SF operation only V05.1 reproduces correctly all the fine features, whereas model V04.1 fails to do so. The main difference can be noted in the position of the CO_3 groups This is due to the difference in the construction of the two models. V05.1 was produced by 180° in-plane rotation of the second block, whereas V04.1 was constructed by the translation of the second block and removal of one CaCO3 layer to produce the observed 3-layer p-ccp stacking across the basal-plane SF in aragonite (Fig. 7).

The visual match is further supported by calculated cross-correlation coefficients (XCC), which are 0.79 and 0.83 for model V04.1 and V05.1, respectively. Although the XCC is low in both cases, reflecting the impaired quality of the experimental image, the difference in XCC is sufficiently large to allow discrimination between these two model variants.

Non-equilibrium stable isotope fractionation, carbonate growth and defects

The question arises as to why (001) SFs occur in Berger Károly cave and Sonnenberg specimens, whereas no such defects were found in the Erzberg sample. To explore this discrepancy, we investigated the stable isotope composition of the samples and evaluated their respective crystallization environments.

The presence of aragonite in the Last Glacial to early Holocene flowstone at Sonnenberg, NW Italy, was attributed to evaporation and concomitant Mg/Ca rise in the parent solution[40]. The carbon and oxygen isotope composition of the calcite-aragonite flowstone[40] indicates ^{13}C and ^{18}O enrichment related to kinetic fractionation due to strong CO_2 degassing, evaporation, and prior calcite precipitation along the water flow route. Strong kinetic fractionation is also supported by the data obtained in the present study (Table S1). The isotopic compositions show a high (r^2 = 0.81) correlation with a slope of 1.7 (Fig. 1J), which indicates kinetic fractionation during carbonate precipitation[47]. As the deposit is hydrologically inactive today, the isotopic composition of the parent water can only be estimated. A nearby modern spring (Stollenquelle, SQ) has a rather constant oxygen isotope composition on a multi-annual timescale (–13.04 ±0.05 ‰[40]). The aragonite and the calcite parts of sample LAS34b from Sonnenberg were drilled close to the FIB lamella and show $\delta^{18}O$ values of –10.5 ±0.2 ‰ and –12.0 ±0.3 ‰, respectively (Table S1). These values are comparable to the results of Koltai et al. [48] obtained for another piece of the same sample.

The stable isotopic composition of the aragonite layer (Table S1) in the Berger Károly cave's calcite encrustation (Figure S1) suggests an aragonite formation mechanism different from that of Sonnenberg. The aragonite has lower $\delta^{13}C$ values (down to –6.0 ‰) than the underlying (–2.7 ‰) and overlying (–3.0 ‰) calcite (Table S1). This depletion indicates that the dissolved inorganic carbon (DIC) of the aragonite-precipitating solution contained organic-derived carbon, consistent with the observed microbial fabric (Fig. S2A).

Aragonite in the Erzberg mine precipitated on calcite in a pool fed by outflow from a borehole[15]. Aragonite formation was related to Mg/Ca increase in the solution due to calcite precipitation[15]. The $\delta^{18}O$ value of the aragonite sample studied here is –8.0 ‰ (Table S1), the water temperature was 5 °C, and the water oxygen isotope composition of the pool water was –10.8 ‰[15].

The $\delta^{18}O$ values, together with the estimated or measured temperatures, were used to calculate oxygen isotope fractionation values (1000·lnα), where the fractionation factor is defined as $\alpha = (1000 + \delta^{18}O_{aragonite})/(1000 + \delta^{18}O_{water})$. The resulting 1000·lnα values were plotted against 1/T (with T in K) in Fig. 1K and compared with the aragonite-water oxygen isotope fractionation equation of Kim et al.[49] ($1000 \cdot \ln\alpha = 17880/T - 31.14$).

The Erzberg sample plots on the equilibrium line, whereas the Sonnenberg and the Berger Károly cave aragonites are offset from equilibrium. However, it should be noted that the water compositions and formation temperatures for the latter fossil occurrences were only estimated using present-day data. If lower temperatures and evaporated water compositions (higher $\delta^{18}O$ water values, see [40]) are used, the fractionation values plot closer to the equilibrium line (as indicated by the arrows in Fig. 1K).

In addition to differences in stable isotope fractionation, the depositional environments of the studied occurrences also differ. The most significant contrast relates to water level. The Erzberg aragonite formed in a pool environment, whereas the Sonnenberg aragonite crystallized from thin water film. Precipitation from a thin water film would have amplified the effects of evaporation and CO_2 degassing, promoting fast carbonate deposition. Microbially mediated carbonate formation – for example in the Berger Károly Cave's aragonite – represents an additional source kinetic driver, as microbial calcite precipitation can further increase the Mg/Ca ratio of the residual solution. In contrast, evaporation and degassing are less effective in subaqueous settings, resulting in diminished kinetic isotope effects[14] - conditions analogous to those inferred for the Erzberg occurrence. Additionally, the location of the Erzberg aragonite site is characterized by the high relative humidity (89 to 100%[15]), which suggests a closed, non-ventilated environment. Thus, the Erzberg aragonite likely precipitated in a relatively stable subaqueous environment, close to oxygen isotopic equilibrium between DIC species and the precipitated aragonite. By comparison, the Sonnenberg and Berger Károly aragonites crystallized under strong kinetic fractionation driven by CO_2 degassing, evaporation, and microbially mediated carbonate precipitation. Although an elevated Mg/Ca ratio appears to have been the primary trigger for aragonite formation in all caves, the degree of Mg-enrichment is different in the studied cases.

The Mg/Ca ratio of the Berger Károly cave sample (L-Top specimen) is 0.034 in the underlying calcite and reaches 0.077 at the top of the microbial-mediated, last-formed calcite (Fig. 1C). The Mg/Ca ratio similarly increases from 0.040 to 0.079 in the Sonnenberg calcite sample (LAS34b specimen) just before aragonite crystallization starts (Fig. 1F). In contrast, the Mg/Ca ratio of the Erzberg sample increases slightly from 0.032 to 0.045 in the last-formed calcite (Fig. 1I). Increasing Mg/Ca ratios can be attributed to Mg enrichment in the solution due to prior calcite precipitation at a low water/carbonate ratio. In the

studied samples Mg is enriched vs Ca in the solution since the Mg/Ca partition coefficient (D = $Mg/Ca_{calcite}/Mg/Ca_{solution}$) is less than 1[50], hence calcite precipitation removes more Ca from the solution relative to Mg. Increased Mg/Ca ratios would be expected for calcite precipitation from a thin water film at low water/carbonate ratios, otherwise a large amount of water would replenish the carbonate-precipitating solution without Mg enrichment vs Ca. The relatively small Mg/Ca change (from 0.032 to 0.045) is in agreement with the pool environment of the Erzberg location. The Mg/Ca ratios indicate that the carbonates of the Sonnenberg and Berger Károly cave locations precipitated from thin water films, where CO_2 degassing and evaporation was more effective and hence disequilibrium kinetic isotope fractionation were more effective than at the Erzberg location.

The observed geochemical features (stable isotope fractionation and Mg/Ca) collectively indicate that the differences in the crystallization environment may explain the well-ordered structure of the Erzberg aragonite versus the presence of ubiquitous stacking faults in the Sonnenberg and Berger Károly samples.

Discussion

Our findings reveal abundant (001) SFs in the first-grown aragonite of the Berger Károly cave and Sonnenberg, and (0001) calcite twins in the last-grown calcite of Sonnenberg. We presume that the lack of (0001) calcite twins in the Berger Károly sample can be explained by the relatively small grain size (50–500 nm) of the microbially precipitated calcite. The atomic structure of the (0001) calcite twin interface corresponds to hexarag, and its occurrence across in the last-grown calcite may record the start of aragonite formation. Structural modelling demonstrates the (001) SFs can be considered as layers of calcite-type (*p-ccp*) Ca stacking sequence with CO_3 groups arranged as in aragonite, inserted parallel to (001) aragonite. Since the structure of the insert layer shows similarities to that of hexarag, we hypothesize that the (001) SF is a relic of the incomplete transformation of this metastable precursor phase to aragonite. Theoretical calculations proposed hexarag as a transitional phase between aragonite and calcite[38], occurring at the nanoscale in an intimate structural relationship with both polymorphs[39]. However, hexarag has not yet been experimentally documented. Although we did not identify hexarag as a bulk phase, our results suggest that it may nonetheless play a role during aragonite formation under specific conditions.

The main factor is that aragonite precipitates from aqueous solutions with elevated molar Mg^{2+}/Ca^{2+} ratio (> 2)[16–18]. As shown above, variations in Mg/Ca molar ratios are also associated with changes in stable isotope fractionation. Stable isotope data indicate that both the Sonnenberg and Berger Károly cave aragonites crystallized from thin water films under conditions of strong kinetic fractionations driven by CO_2 degassing, evaporation, and microbial carbonate precipitation, i.e., under isotopically non-equilibrium conditions. In contrast, the Erzberg aragonite precipitated subaqueously in a relatively constant physicochemical environment, close to isotopic equilibrium; consistently, no evidence for (001) SFs was detected in this sample. Therefore, we infer that non-equilibrium crystallization conditions may

favor the formation of hexarag and its incomplete transformation, preserved as (001) aragonite SFs and (0001) calcite twins. This interpretation implies that such defects may be common in the early-formed aragonite overgrowing calcite in dynamically evolving geologic environments.

Figure 8 shows a conceptual model illustrating how kinetic effects drive the rapid formation of hexarag, which subsequently evolves into calcite twins and (001) aragonite SFs. The fast deposition of the Berger Károly and the Sonnenberg aragonites, as inferred from their stable isotope composition, is consistent with the observed variations in Mg/Ca ratios. Aragonite precipitation occurs when the Mg/Ca ratio of the parent solution exceeds 2:1, a condition reflected by the increase from 0.032 to 0.045 measured in the calcite substrate underlying the Erzberg aragonite. In contrast, the Berger Károly and Sonnenberg deposits show a more pronounced increase in Mg/Ca ratios within the underlying calcite, from 0.034 and 0.044 to 0.077 and 0.079, respectively. We interpret this elevated Mg/Ca signal as a kinetic “overshoot”, indicating that the solution compositions rapidly exceeded the threshold required for aragonite precipitation.

The identification of (001) aragonite SFs can be challenging, as it requires careful sample preparation and detailed SAED and HRTEM measurements. TEM lamella preparation across the aragonite-calcite interface and proper < 100 > and/or < 110 > orientations of the sample are required. The diffraction contribution of SFs, i.e., streaking of 001 aragonite reflections, may be weak and difficult to notice in SAED patterns, which could explain why these defects have not been identified previously. However, samples with apparent (001) aragonite // (0001) calcite intergrowths represent prime candidates for identifying (001) aragonite SFs and (0001) calcite twins, and thus for inferring the presence of a hexarag precursor phase. Such samples have been reported in geologic samples[51–52]. These occurrences provide promising targets for the identification of (001) aragonite SFs and for testing the proposed link between defects and non-equilibrium crystallization conditions.

Our study demonstrates that (001) SFs in aragonite are consistent with the insertion of calcite-type slabs within the (001) aragonite structure. Whereas aragonite is characterized by 9-fold coordinated Ca sites, calcite-like slabs embedded in aragonite may accommodate foreign elements that preferentially occupy 6-coordinated sites, such as Mg, Cu, Zn or Co. Mg, for instance, could potentially be incorporated in early-formed aragonite, although we did not detect significant Mg enrichment in our samples. Transition metals are known to impart color to aragonite[53–54], and their incorporation may likewise be associated with (001) aragonite SFs.

Certain bivalves grow calcite in the outer (prismatic) shell layer, while the inner (nacre) layer is aragonite[55–56]. Such polymorph selection is commonly explained by the influence of organic matrix macromolecules that regulate nucleation, crystal growth, and local chemical conditions[22, 57–58]. However, Bruno et al.[39] suggested that the growth of the calcite outer layer can be associated with the formation of hexarag at the aragonite-calcite epitaxial interface. We propose that these mollusks’ layers could also be candidates for finding (001) aragonite SFs and the study of these transitional structures could contribute to a better understanding of the polymorph selections in mollusks.

Methods

Samples

The studied samples have been described in detail by Koltai et al. (48, Sonnenberg), Eichinger et al.[15] (Erzberg), and Demény et al.[14] (Berger Károly cave). The Berger Károly cave is situated beneath the town of Tapolca (western Hungary, N 46° 53’ 14”, E 17° 26’ 30”, Fig. S1a). It is strictly protected, and only expert cavers can enter with the permission of the Balaton Uplands National Park (see Acknowledgements). A drill core was taken from the calcite deposit of lake Lángos within the cave in 2021, and the studied sample was taken from the top of the core (L-top, Fig.S1b). The temperature of the pool water was 24.3°C[14], and the cave air temperature was about 15°C (ranging from 13 to 17°C depending on the actual location within the cave during the measurements in February and July 2022). A 1 mm-thin, white carbonate crust is present on the top of the drill core, consisting of needle-like aragonite crystals at its base, overlain by isometric calcite crystals[14].

The Sonnenberg site is located on the south-facing slope of the Vinschgau valley (Val Venosta) in northern Italy (N 46° 37' 48", E 10° 40' 59") (Fig. S1a). The aragonite sample (LAS 34b; “b” indicates that the sample is a piece of the LAS34 sample of 48) was obtained from a vein-lining flowstone formed in a cavity of metamorphic rocks[14]. The sample is dominated by mosaic calcite where fascicular optic calcite polycrystals are locally present between acicular aragonite and fascicular optic calcite.

The Erzberg iron ore deposit (central Austria, N 47°31'30", E 14°54'42") is situated in the Northern Graywacke Zone (Fig. S1a). The studied sample was collected from the historic adit called “Presserstollen”[15], where a thick carbonate deposit formed in an artificial pool from inflowing groundwater. The sample was collected in the central area of this shallow pool[15].

Characterization methods, modeling, and calculations

Optical and scanning electron microscopy

Transmitted light optical microscopy of thin sections was performed using a Nikon Eclipse E600 optical microscope on polished samples. The samples were carbon-coated and were also imaged using a JEOL JSM-IT700HR scanning electron microscope operated at 20 kV equipped with a backscattered electron detector. Chemical compositions were acquired using the built-in JEOL energy-dispersive X-ray spectrometer, and data were quantified following ZAF correction.

Sample preparation and transmission electron microscopy

Approximately 4x2 µm areas from selected grains were cut and thinned by focused ion-beam (FIB) using a Thermo Scientific Scios 2 instrument. The FIB lamellae were investigated with a FEI Talos F200X G2 scanning transmission electron microscope operated at 200 kV. The microscope was used for recording

both low-magnification bright-field (BF) TEM images, as well as high-resolution (HR) TEM images, low-magnification HAADF STEM images, atomic resolution STEM HAADF images, and corresponding SAED patterns. For the atomic resolution STEM HAADF image acquisition, a fast scan (500 ns dwell time) and low beam current (~ 12 pA) were applied, and series of 50 or 100 frames were collected and summed with Thermo Scientific Velox software using a cross-correlation drift correction method (DCFI). Fast Fourier transforms (FFTs) were calculated using Gatan Digital Micrograph 3.6.1 software.

Structure modeling

Basal-plane SFs in aragonite were constructed using structure modeling software[59] (CrystalMaker® Software Ltd., Oxfordshire, UK). To address the breakdown of spatial periodicity along the c-axis due to translations generated by the planar defect (SF), double SF models were constructed, where the second SF of identical local structure and translation serves to rectify the original translation, whereby the supercells regain c-axis periodicity[60]. Such models can be used in calculations that necessitate fully periodic objects (crystals). Rigid structure models were used for quantum chemical calculations. DFT-optimized structures were used for simulating HAADF-STEM images that were matched with experimental HAADF-STEM images for an identification of the model with the highest cross-correlation (XCC) coefficient.

DFT structure optimization

Energetic optimizations of the structures were performed within the density functional theory (DFT) implemented in the VASP package[61–62]. The exchange-correlation interaction was taken into account in the generalized gradient approximation in the form of the Perdew-Burke-Ernzerhof (PBE) functional[63]. Valence electrons were represented with a plane wave basis set with a cutoff energy of 800 eV. The valence configurations have been chosen as Ca($2p^6 3s^2$), C ($2s^2 2p^2$), and O ($2s^2 2p^4$). The Brillouin zone was sampled by a Γ-centered Monkhorst-Pack[64] k-point grid of spacing of 0.2 $Å^{-1}$ and σ = 0.05 eV. As a reference the following crystal structures have been used for calculations: calcite[65], aragonite[66], and hexarag[39].

To examine the thermal stability of the V05.1 structure, DFT-based ab initio molecular dynamics (MD) simulations were performed using a supercell with 216 atoms at 350 K. The time step was set to 1 fs. The total simulation time was 20 ps. The NPT ensemble (N for the number of particles, P for pressure, and T for temperature) was used. During the simulation, the frequency of the temperature oscillations was controlled by the Langevin thermostat.

Stable isotope measurements

Stable carbon and oxygen isotope compositions were determined using an automated carbonate preparation device (Gasbench II) coupled to a Thermo Finnigan Delta plus XP continuous-flow mass

spectrometer at the Institute for Geological and Geochemical Research, HUN-REN Research Centre for Astronomy and Earth Sciences. Three laboratory standards, calibrated using the NBS-18, NBS-19 and LSVEC reference materials, were used for sample standardization. The isotope compositions are expressed as δ13C and δ18O values (in ‰) relative to V-PDB. A standard calcite called Harding Iceland Spar (67) was analyzed as unknown in the course of this study that yielded $\delta^{13}C = -4.86 \pm 0.06‰$ and $\delta18O = -18.50 \pm 0.02‰$ (n = 8) in close agreement with the expected compositions ($\delta^{13}C = -5.80‰$, $\delta18O = -18.56‰$[67]), demonstrating measurement accuracy. Phosphoric acid fractionation factors of Kim et al.[68] were used for the analyses..

Declarations

Acknowledgements (optional)

Sampling in Berger Károly Cave was carried out with permission from the directorate of the Balaton Uplands National Park (No. 102-2/2022). Rezső Szilaj, Ágnes Berentés, and Gergely Surányi provided essential help during sampling. The work was supported by grants ANN 141894, SNN-139585, and RRF-2.3.1-21-2022-00014 from the National Research, Development and Innovation Office. PNG and MVB were supported by the Russian Science Foundation, project no. 25-23-00076 (https://rscf.ru/project/25-23-00076/).

Data Availability

All data are available in the main text or the supplementary information.

References

1. J.W. Morse, F.T. Mackenzie, Geochemistry of Sedimentary Carbonates, Dev. in Sedimentology, 48, 707 p., Amsterdam (Elsevier) (1990).
2. S. Frisia, A. Borsato, I.J. Fairchild, F. McDermott, E.M. Selmo, Aragonite-calcite relationships in speleothems (Grotte de Clamouse, France): Environment, fabrics, and carbonate geochemistry. J. Sediment. Res. 72 (5), 687–699 (2002). https://doi.org/10.1306/020702720687
3. N.P. James, B. Jones, Origin of carbonate sedimentary rocks, Chichester (Wiley). (2016)
4. M. Dietzel, R. Boch, Precipitation of CaCO3 in natural and man-made aquatic environments - Mechanisms, analogues, and proxies. Geochemistry 84, 126206 (2024). https://doi.org/10.1016/j.chemer.2024.126206
5. C.A. Hill, P. Forti, Cave Minerals of the World (2nd ed.). National Speleological Society, Huntsville, USA. (1997).
6. A. Immenhauser et al., Petrographic and geochemical constraints on the formation of gravity-defying speleothems. The Depositional Record 9(3), 413–436 (2023).

https://doi.org/10.1002/dep2.199

7. B. Jones, R.W. Renaut, Morphology and growth of aragonite crystals in hot-spring travertines at Lake Bogoria, Kenya Rift Valley, Sedimentology 43, 323–340 (1996). https://doi.org/10.1046/j.1365-3091.1996.d01-7.x
8. M. Herrero et al., Hydrothermal activity within a sedimentary succession: Aragonites as indicators of Mesozoic Rifting (Iberian Basin, Spain). Int. Geol. Rev. 62, 94–112 (2020). https://doi.org/10.1080/00206814.2019.1636317
9. E. Vetrov et al., The middle paleozoic magmatism of the central tuvinian trough (eastern altai-sayan fold area): Petrogenesis, tectonics, and geodynamics. Russ. Geol. Geophys. 63, 1333–1353 (2022). https://doi.org/10.2113/RGG20214379
10. R. Boch et al., Aragonite–calcite veins of the 'Erzberg' iron ore deposit (Austria): Environmental implications from young fractures. Sedimentology 66(2), 604–635 (2019). https://doi.org/10.1111/sed.12500
11. G. Falini, S. Albeck, S. Weiner, L. Addadi, Control of aragonite or calcite polymorphism by mollusk shell macromolecules. Science 271, 67–69 (1996). https://doi.org/10.1126/science.271.5245.6
12. G.A. Farfan et al., Crystallographic and chemical signatures in coral skeletal aragonite. Coral Reefs 41(1), 19–34 (2022). https://doi.org/10.1007/s00338-021-02198-4
13. K. Benzerara, A. Meibom, Q. Gautieri, J. Kazmierczk, J. Stolarski, N. Menguyi, G. Brown, Nanotextures of aragonite in stromatolites from the quasi-marine Satonda crater lake, Indonesia. From: Pedley, H. M. & Rogerson, M. (eds) Tufas and Speleothems: Unravelling the Microbial and Physical Controls. Geological Society, London, Special Publications, 336, 211–224 (2010). https://doi.org/10.1144/SP336.1
14. A. Demény, Á. Berentés, L. Rinyu, I. Kovács, G. Surányi, M. Virág, Subaqueous carbonate speleothems as paleotemperature archives – clumped isotope thermometry and stable isotope compositions of inclusion-hosted water. International Journal of Speleology 53(1), 25–37 (2024). https://doi.org/10.5038/1827-806X.53.1.2480
15. S. Eichinger et al., Unravelling calcite-to-aragonite evolution from a subsurface fluid - formation pathway, interfacial reactions and nucleation effects. Chem. Geol. 641, 121768 (2023). https://doi.org/10.1016/j.chemgeo.2023.121768
16. V. De Choudens-Sánchez, L.A. González, Calcite and aragonite precipitation under controlled instantaneous supersaturation: elucidating the role of CaCO3 saturation state and Mg/Ca ratio on calcium carbonate polymorphism. J. Sed. Res. 79, 363–376 (2009). https://doi.org/10.2110/jsr.2009.043
17. B. Jones, Review of aragonite and calcite crystal morphogenesis in thermal spring systems. Sedim. Geol. 54, 9–23 (2017). https://doi.org/10.1016/j.sedgeo.2017.03.012
18. R.L. Folk, Interaction between bacteria, nannobacteria, and mineral precipitation in hot springs in central Italy. Géog. Phys. Quat. 48, 233–246 (1994). https://doi.org/10.7202/033005ar

19. S. Riechelmann, Physicochemical characteristics of drip waters: Influence on mineralogy and crystal morphology of recent cave carbonate precipitates. Geochim. Cosmochim. Acta 145, 13–29 (2014). https://doi.org/10.1016/j.gca.2014.09.019
20. V. Mavromatis, J.M. Brazier, K.E. Goetschl, Controls of temperature and mineral growth rate on Mg incorporation in aragonite. Geochim. Cosmochim. Acta 317, 53–64 (2022). https://doi.org/10.1016/j.gca.2021.10.015
21. W. Sun, Nucleation of metastable aragonite CaCO3 in seawater. Proc. Natl. Acad. Sci. U.S.A. 112 (11), 3199–3204 (2015). https://doi.org/10.1073/pnas.1423898112
22. G. Falini, Control of aragonite or calcite polymorphism by mollusk shell macromolecules. Science 271, 67–69 (1996). https://doi.org/10.1126/science.271.5245.67
23. H.H. Teng, P.M. Dove, C.A. Orme, J.J. De Yoreo, Thermodynamics of calcite growth: Baseline for understanding biomineral formation. Science 282,724–727 (1998). https://doi.org/10.1126/science.282.5389.724
24. O. Nahi, et al., Polyamines promote aragonite nucleation and generate biomimetic structures, Adv. Sci. 10, 1–12 (2023). https://doi.org/10.1002/advs.202203759
25. T. Mass et al., Amorphous calcium carbonate particles form coral skeletons. Proc. Natl. Acad. Sci. U.S.A. 114, E7670 – E7678 (2017). https://doi.org/10.1073/pnas.1707890114
26. R.T. DeVol, C.-Y. Sun, M.A. Marcus, S.N. Coppersmith, S.C.B. Myneni, P.U.P.A Gilbert, Nanoscale transforming mineral phases in fresh nacre. J. Am. Chem. Soc. 137, 13325–13333 (2015). https://doi.org/10.1021/jacs.5b07931
27. K.K. Sand, J.D. Rodriguez-Blanco, E. Makovicky, L.G. Benning, S.L.S. Stipp, Crystallization of CaCO3 in water–alcohol mixtures: Spherulitic growth, polymorph stabilization and morphology change. Cryst. Growth Des. 12, 842–853 (2012). https://doi.org/10.1021/cg2012342
28. M. Farhadi-Khouzani, D. M. Chevrier, P. Zhang, N. Hedin, D. Gebauer, Water as the key to proto-aragonite amorphous CaCO3. Angew. Chem. Int. Ed. Engl. 55, 8117–8120 (2016). https://doi.org/10.1002/anie.201603176
29. J. M. Walker, B. Marzec, F. Nudelman, Solid-state transformation of amorphous calcium carbonate to aragonite captured by cryoTEM. Angew. Chem. Int. Ed. Engl. 56, 11740–11743 (2017). https://doi.org/10.1002/anie.201703158
30. Z. Molnár, P. Pekker, A. Rečnik, M. Pósfai, Formation and properties of spindle-shaped aragonite mesocrystals from Mg-bearing solutions. Nanoscale 16, 2012–2021 (2024). https://doi.org/10.1039/D3NR04672A
31. A. V. Radha, T.Z. Forbes, C.E. Killian, P.U.P.A Gilbert, A. Navrotsky, Transformation and crystallization energetics of synthetic and biogenic amorphous calcium carbonate. Proc. Natl. Acad. Sci. U.S.A. 107, 16438–16443 (2010). https://doi.org/10.1073/pnas.1009959107
32. T. Ogino, T. Suzuki, K. Sawada, K., The formation and transformation mechanism of calcium carbonate in water. Geochim. Cosmochim. Acta 51, 2757–2767 (1987). https://doi.org/10.1016/0016-7037(87)90155-4

33. T. Munemoto, K. Fukushi, Transformation kinetics of monohydrocalcite to aragonite in aqueous solutions. J. Mineral. Petrol. Sci. 103, 345–349 (2008). https://doi.org/10.2465/jmps.080619
34. M. Suyama, T. Kitajima, K. Fukushi, Solubility of calcium carbonate hemihydrate (CCHH): Where does CCHH occur? Geochem. Persp. Let. 31, 27–31 (2024). https://doi.org/10.7185/geochemlet.2428
35. A. Lázár, A. Demény, I. Hegyi, L.E. Aradi, L.A.J. Garvie, P. Németh, Oxygen isotopic re-equilibration during transformation of ikaite to calcite via amorphous calcium carbonate. Chem. Geol. 693, 122980 (2025). https://doi.org/10.1016/j.chemgeo.2025.122980
36. P. Németh, E. Mugnaioli, M. Gemmi, G. Czuppon, A. Demény, C. Spötl, A nanocrystalline monoclinic CaCO3 precursor of metastable aragonite. Sci. Adv. 4, eaau6178 (2018). https://doi.org/10.1126/sciadv.aau6178
37. P.N. Gavryushkin et al., The intrinsic twinning and enigmatic twisting of aragonite crystals. Proc. Natl. Acad. Sci. U.S.A. 121(6), e2311738121 (2024). https://doi.org/10.1073/pnas.2311738121
38. P.N. Gavryushkin et al., Metastable structures of CaCO3 and their role in transformation of calcite to aragonite and postaragonite. Cryst. Growth Des. 21, 65–74 (2021). https://doi.org/10.1021/acs.cgd.0c00589
39. M. Bruno, M. Prencipe, D. Aquilano, A. Cotellucci, S. Ghignone, P. Németh, Calcite/aragonite epitaxy: a computational study for understanding mollusk shell formation. J. Phys. Chem. C 126 (14), 6472–6481 (2022). https://doi.org/10.1021/acs.jpcc.2c00785
40. C. Spötl, M. Unterwurzacher, A. Mangini, F.J. Longstaffe, Carbonate speleothems in the dry, inneralpine Vinschgau valley, northernmost Italy: witnesses of changes in climate and hydrology since the Last Glacial Maximum, J. Sediment. Res. 72, 793–808 (2002). https://doi.org/10.1306/041102720793
41. B. Jones, X. Peng, Amorphous calcium carbonate associated with biofilms in hot spring deposits. Sedim. Geol. 269–270, 58–68 (2012). https://doi.org/10.1016/j.sedgeo.2012.05.019
42. N.T. Enyedi et al., Cave bacteria-induced amorphous calcium carbonate formation. Scientific Reports 10, 8696 (2020). https://doi.org/10.1038/s41598-020-65667-w
43. J.M. McCrea, On the isotopic chemistry of carbonates and a paleotemperature scale. J. Chem. Phys. 18, 849–857 (1950). https://doi.org/10.1063/1.1747785
44. V. Ribić et al., New inversion boundary structure in Sb-doped ZnO predicted by DFT calculations and confirmed by experimental HRTEM. Acta Mater. 199, 633–648 (2020). https://doi.org/10.1016/j.actamat.2020.08.035
45. M. Bruno, F.R. Massaro, M. Rubbo, M. Prencipe, D. Aquilano, (10.4), (01.8), (01.2), and (00.1) Twin Laws of Calcite (CaCO3): Equilibrium Geometry of the Twin Boundary Interfaces and Twinning Energy. Cryst. Growth Des. 10, 3102–3109 (2010). https://doi.org/10.1021/cg100233p
46. A. Rečnik, G. Möbus, S. Šturm, IMAGE-WARP: A real-space restoration method for high-resolution STEM images using quantitative HRTEM analysis. Ultramicroscopy 103, 285–301 (2005). https://doi.org/10.1016/j.ultramic.2005.01.003

47. P.J. Mickler, L.A. Stern, J.L. Banner, Large kinetic isotope effects in modern speleothems. GSA Bulletin 118, 65–81 (2006). https://doi.org/10.1130/B25698.1
48. G. Koltai, H. Cheng, C. Spötl, Palaeoclimate significance of speleothems in crystalline rocks: a test case from the Late Glacial and early Holocene (Vinschgau, northern Italy). Clim. Past. 14, 369–381 (2018). https://doi.org/10.5194/cp-14-369-2018
49. S.-T. Kim, J.R. O'Neil, C. Hillaire-Marcel, A. Mucci, Oxygen isotope fractionation between synthetic aragonite and water: Influence of temperature and Mg2 + concentration. Geochim. Cosmochim. Acta 71, 4704–4715 (2007). https://doi.org/10.1016/j.gca.2007.04.019
50. Y. Huang, I.J. Fairchild, Partitioning of Sr2 + and Mg2 + into calcite under karst-analogue experimental conditions. Geochim. Cosmochim. Acta 65, 47–62 (2001). https://doi.org/10.1016/S0016-7037(00)00513-5
51. D.R. Dasgupta, The oriented transformation of aragonite into calcite. Mineral. Mag. J. Mineral. Soc., 33, 924–928 (1964). https://doi.org/10.1180/minmag.1964.033.265.09
52. S. Bruni Frisia, H.R. Wenk, Replacement of aragonite by calcite in sediments from the San Cassiano formation (Italy). J. Sediment. Petrol. 55, 159–170 (1985). https://doi.org/10.1306/212F8652-2B24-11D7-8648000102C1865D
53. G.A. Caddeo, W. Jo De, F. Franco, B.R. Loren B.R., Trace element and stable isotope data from a flowstone in a natural cave of the mining district of SW Sardinia (Italy): evidence for Zn^{2+}-induced aragonite precipitation in comparatively wet climatic conditions. Intern. J. Speleol., 40, 181–190 (2011). http://dx.doi.org/10.5038/1827-806X.40.2.10
54. M. Vlieghe et al., Polymetallic interactions of Zn-Pb-Cu in blue/green-colored speleothems from Malaval Cave (France). Geochemistry, 126285 (2025). https://doi.org/10.1016/j.chemer.2025.126285
55. Y. Dauphin et al., Structure and composition of the nacre-prisms transition in the shell of Pinctada margaritifera (Mollusca, Bivalvia). Anal. Bioanal. Chem. 390, 1659–1669 (2008). https://doi.org/10.1007/s00216-008-1860-z
56. T. Okumura, M. Suzuki, H. Nagasawa, T. Kogure, Characteristics of biogenic calcite in the prismatic layer of a pearl oyster, Pinctada fucata. Micron 41, 821–826 (2010). https://doi.org/10.1016/j.micron.2010.05.004
57. F. Marin, N. Le Roy, B. Marie, B., The formation and mineralization of mollusk shell Frontiers in Bioscience 4(3), 1099–125 (2012). https://doi.org/10.2741/s321
58. L. Addadi, D. Joester, F. Nudelman, S. Weiner, Mollusk shell formation: a source of new concepts for biomineralization. Chemistry - A European Journal 12(4), 980–987 (2012). https://doi.org/10.1002/chem.200500980
59. D.C. Palmer, Visualization and analysis of crystal structures using CrystalMaker software. Z. Kristallogr. 230(9–10), 559–572 (2015). https://doi.org/10.1515/zkri-2015-1869
60. V. Ribić, V. Jordan, S. Drev, J. Kovač, G. Dražić, A. Rečnik, Mnemonic rutile–rutile interfaces triggering spontaneous dissociation of water. Adv. Mater. 36, 2308027 (2024).

https://doi.org/10.1002/adma.202308027

61. G. Kresse, J. Furthmüller, Efficient iterative schemes for ab initio total-energy calculations using a plane-wave basis set. Phys. Rev. B 54(16), 11169 (1996). https://doi.org/10.1103/PhysRevB.54.11169
62. G. Kresse, D. Joubert, From ultrasoft pseudopotentials to the projector augmented-wave method. Phys. Rev. B 59(3), 1758–1775 (1999). https://doi.org/10.1103/PhysRevB.59.1758
63. J.P. Perdew, K. Burke, M. Ernzerhof, Generalized gradient approximation made simple. Phys. Rev. Lett. 77(18), 3865 (1996). https://doi.org/10.1103/PhysRevLett.77.3865
64. H.J. Monkhorst, J.D. Pack, Special points for Brillouin-zone integrations. Phys. Rev. B 13(12), 5188 (1976). https://doi.org/10.1103/PhysRevB.13.5188
65. D.L. Graf, Crystallographic tables for the rhombohedral carbonates. Amer. Mineral. 46(11–12), 1283–1316 (1961).
66. E.N. Caspi, B. Pokroy, P.L. Lee, J.P. Quintana, E. Zolotoyabko, On the structure of aragonite. Acta Cryst. Section B, 61, 129–132 (2005). https://doi.org/10.1107/S0108768105005240
67. G.P. Landis, Harding Iceland spar: A new δ18O – δ13C carbonate standard for hydrothermal minerals. Chem. Geol. 41, 91–94 (1983). https://doi.org/10.1016/S0009-2541(83)80008-4.
68. S.-T. Kim, A. Mucci, B.E. Taylor, Phosphoric acid fractionation factors for calcite and aragonite between 25 and 75°C: Revisited. Chem. Geol. 246, 135–146 (2007). https://doi.org/10.1016/j.chemgeo.2007.08.005

Table

Table 1. Calculated enthalpies of different CaCO3 structures

Phase	Enthalpy (H), eV	N f.u. (Z)	H/Z	H-H(arag)
calcite	-222.617	6	-37.103	-0.153
hexarag	-74.067	2	-37.033	-0.084
aragonite	-147.799	4	-36.950	0.000
V05.1	-1771.643	48	-36.909	0.040
V04	-1771.515	48	-36.907	0.043
V06	-1769.694	48	-36.869	0.081
V05.2	-1765.719	48	-36.786	0.164

Figures

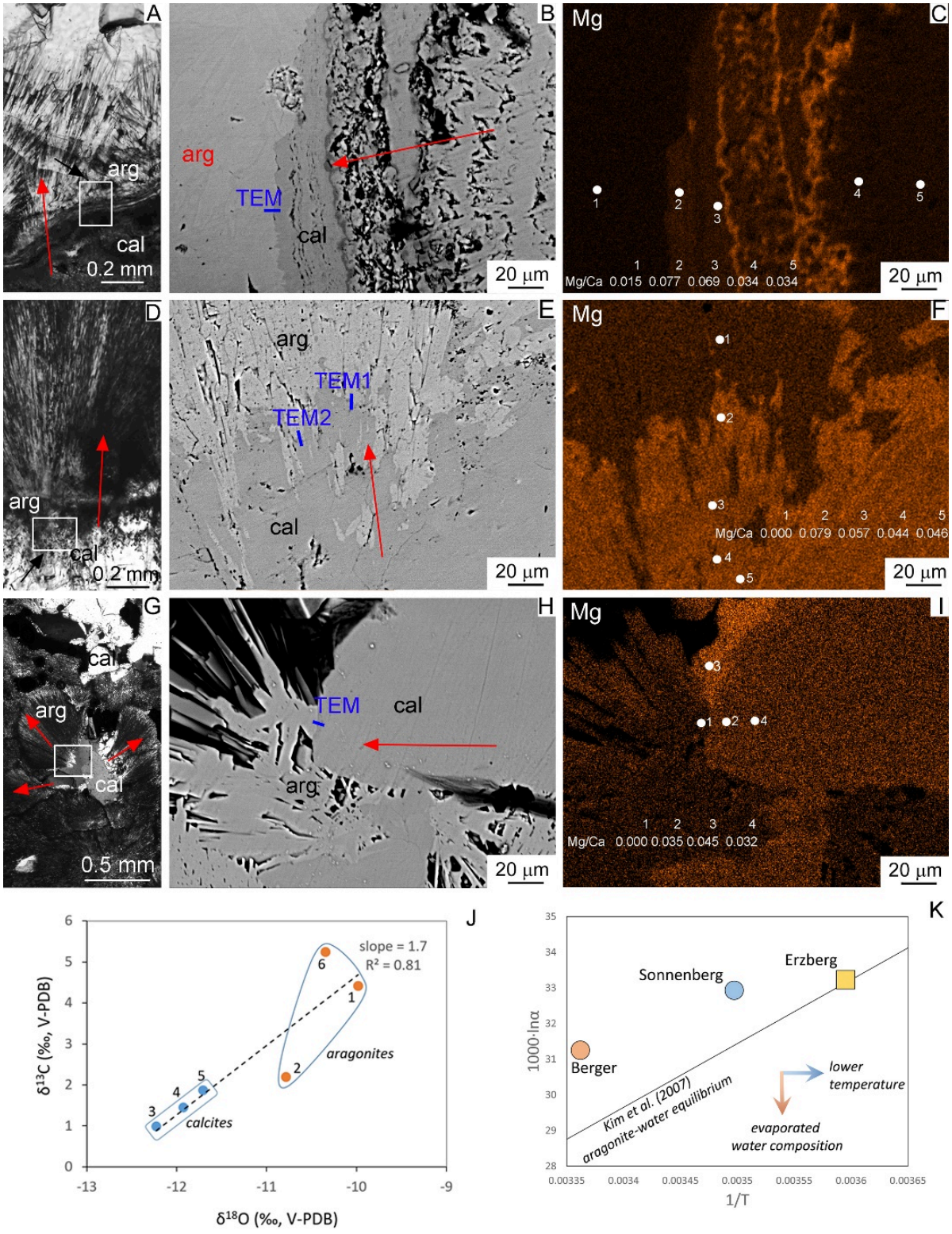


Figure 1

Aragonite (arg) – calcite (cal) interfaces in samples of the Berger Károly cave (A-C), Sonnenberg (D-F), and Erzberg (G-I) and their oxygen isotope data (J, K). A, D, G: Transmitted-light microscope images. Red arrows point to the direction of growth, and white rectangles mark the magnified areas. B, E, H: BSE images. Blue lines mark the sites selected for TEM analysis. C, F, I: Mg distribution maps and selected Mg/Ca values (atomic %) across the interface, obtained from EDS point analysis. J: Stable carbon and

oxygen isotope compositions of calcite and aragonite subsamples of sample LAS34b (LAS34b1 – 6, see Table S1). K: Oxygen isotope fractionation (1000lnα values) as a function of temperature (where T is in K) for aragonite from the Erzberg mine[15], the Sonnenberg site (sample LAS 34b, see also[40, 48]) and the Berger Károly cave (sample L-top, [14]). The arrows indicate the effects of uncertainties in the estimated water compositions and precipitation temperature (see main text).

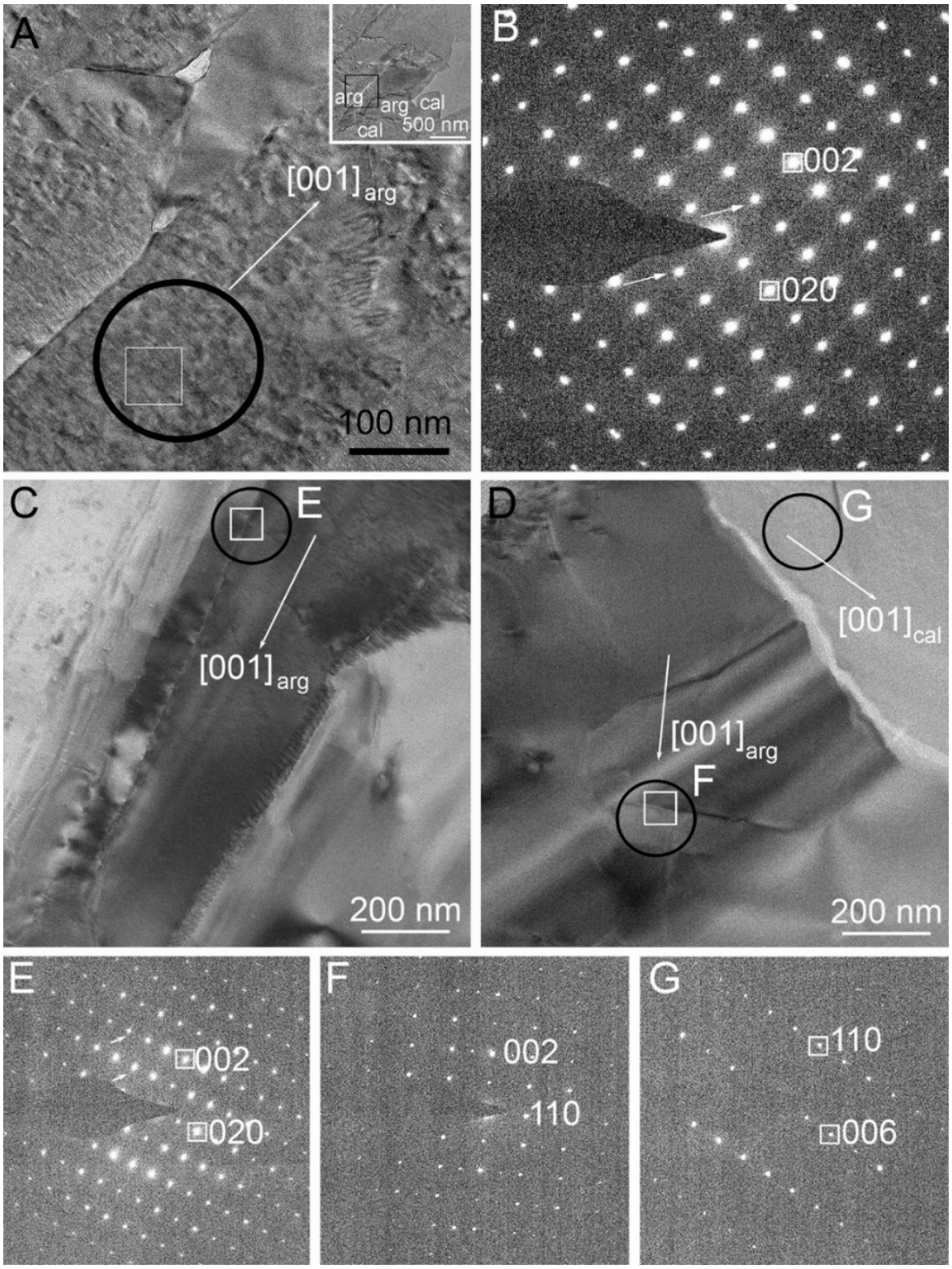


Figure 2

Nanostructures of the aragonite-calcite interface in samples from Berger Károly cave (A, B), Sonnenberg (C, E) and Erzberg (D, F, G). A: BFTEM image of the first-grown aragonite on calcite from Berger Károly cave (TEM, Fig. 1B), obtained from the area marked by a black rectangle (insert, Fig. S3). White rectangle marks the area of Fig. 3A. B: SAED pattern, taken from the area within the black circle in A, shows aragonite viewed along [100]. White arrows point to streaked reflections. C: BFTEM image of the first grown aragonite from Sonnenberg (TEM1, Fig. 1E). D: TEM image of the first grown aragonite and last grown calcite from Erzberg. Black circles and white rectangles mark areas studied by SAED (E, F, G) and HRTEM images in Fig. S5, S6. E, F: Aragonite viewed along [100] and [1 0], respectively. White arrows point to streaked reflections in E. G: Calcite viewed along [1 0].

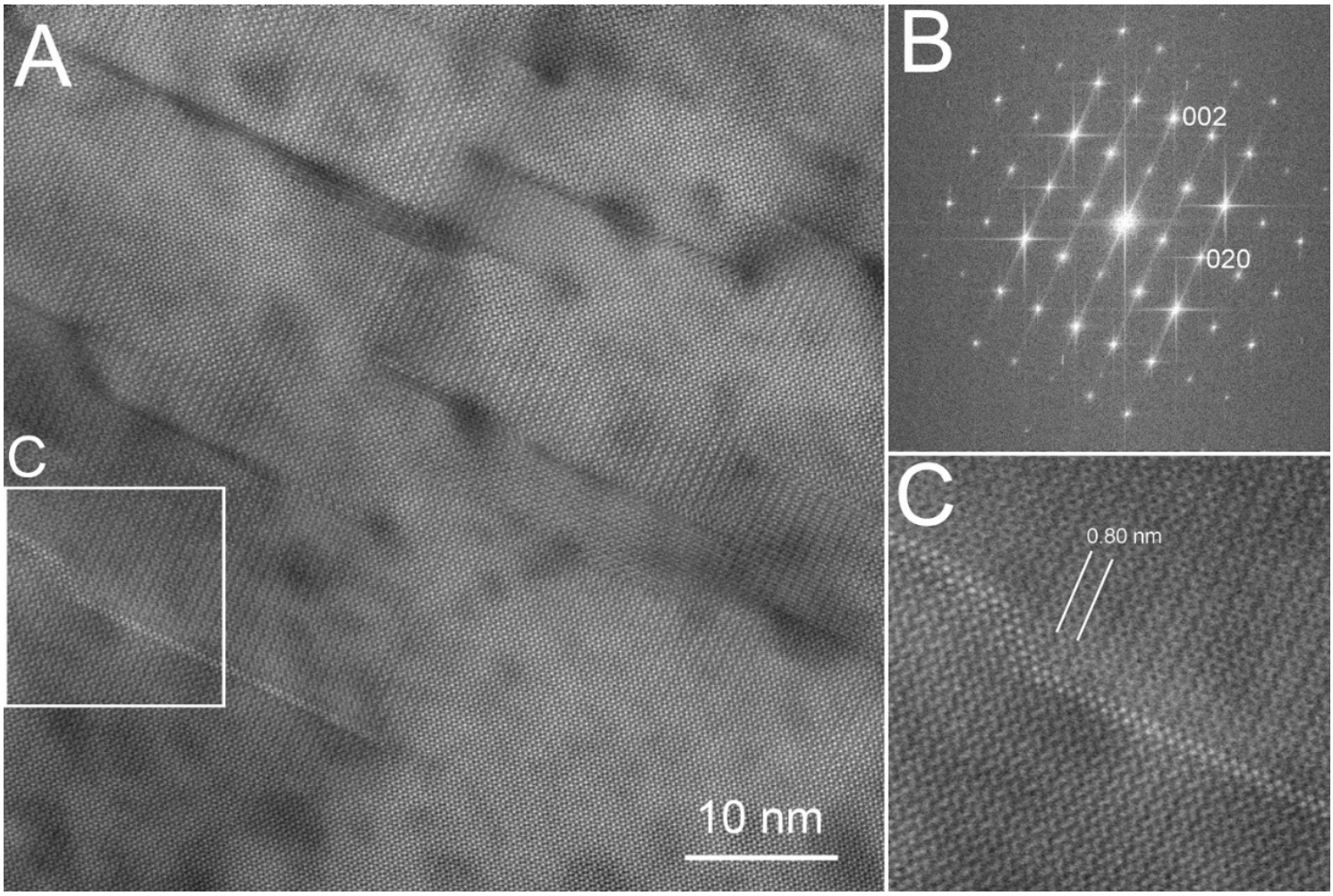


Figure 3

High density of (001) SFs in first-grown aragonite from Berger Károly cave. A: HAADF STEM image of (001) SFs in aragonite. White rectangle marks the area of Fig. 3C. B: FFT calculated from area A. C: Magnified area of a single (001) SF from A.

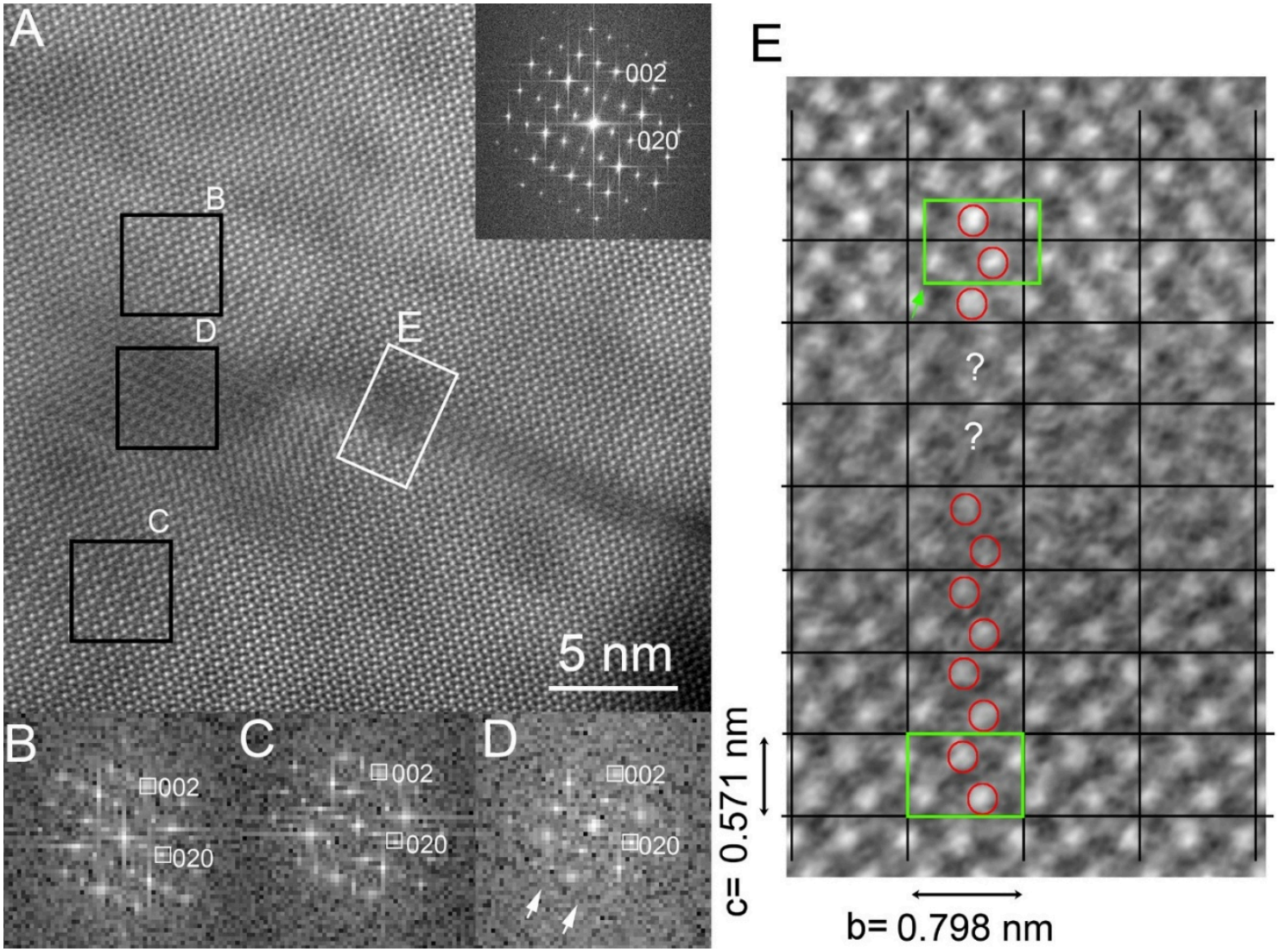


Figure 4

Lattice translation across a (001) SF (Berger Károly cave). A: HAADF STEM image of the SF. B, C, D: FFTs calculated from selected regions of A. White arrows point to systematic absences for *k*= 2*n*+1 on (0*kl*). E: Enlarged and 24°-rotated view of a segment of a SF, showing a lattice shift (green arrow) corresponding to ~1/6b+1/2c relative to a reference grid extended from bottom domain (black). Red circles indicate approximate positions of Ca-columns in both domains. The regular p-*hcp*sequence of aragonite is disrupted across the interface.

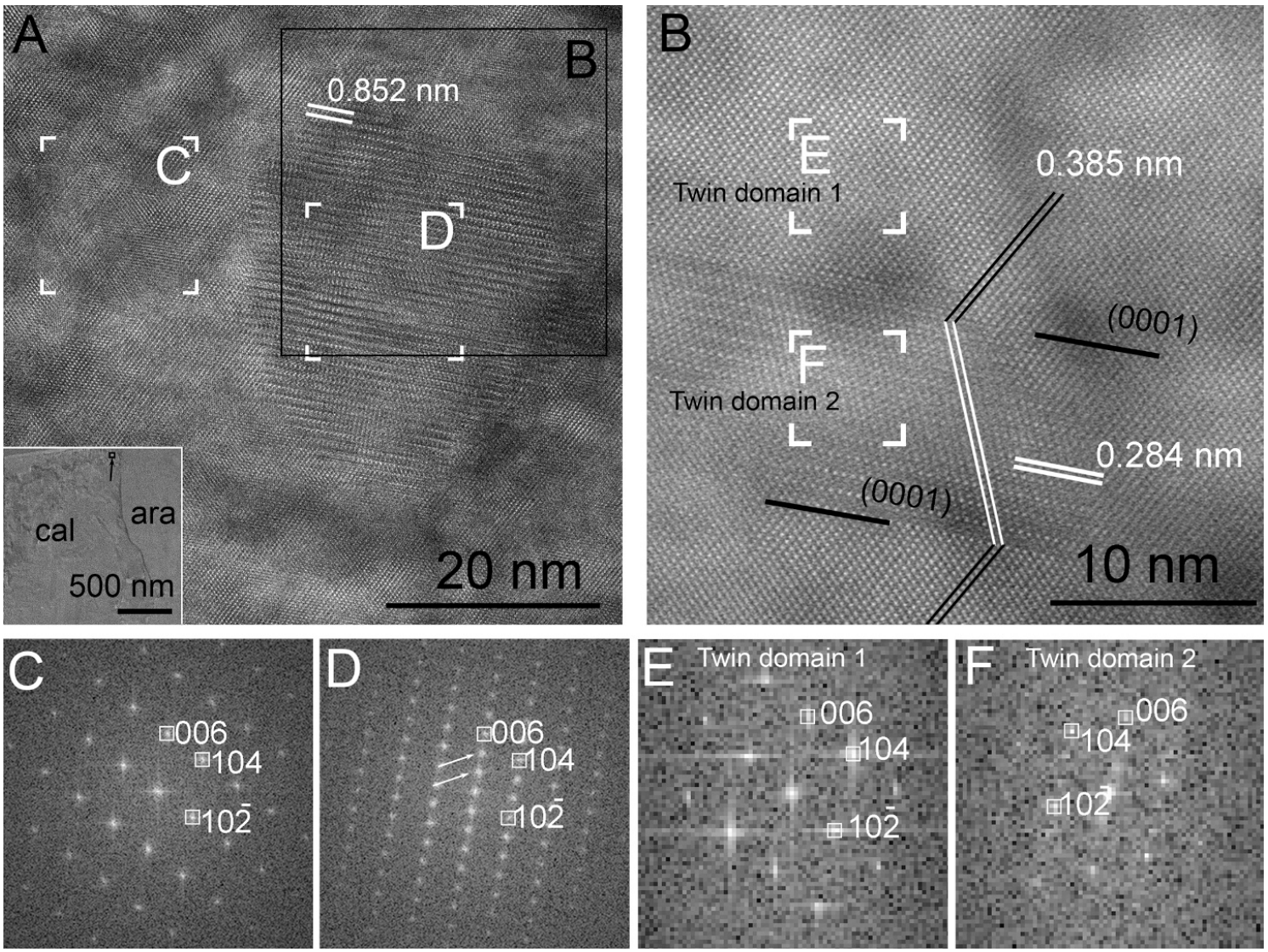


Figure 5

(0001) twins in the last-grown calcite (Sonnenberg) projected along [010] . A: HRTEM image with triple d006 calcite spacings from the area marked as TEM2 in Fig. 1E. Bottom left insert shows a BFTEM image, and the black arrow points to the investigated area. B: HR HAADF STEM image with (0001) double twinned domains. Black and white lines mark the spacings of the two twin domains. C, D, E, F: FFTs calculated from selected regions of A and B. White arrows in D mark reflections arising from the superposition of double twinned domains (Fig. S6).

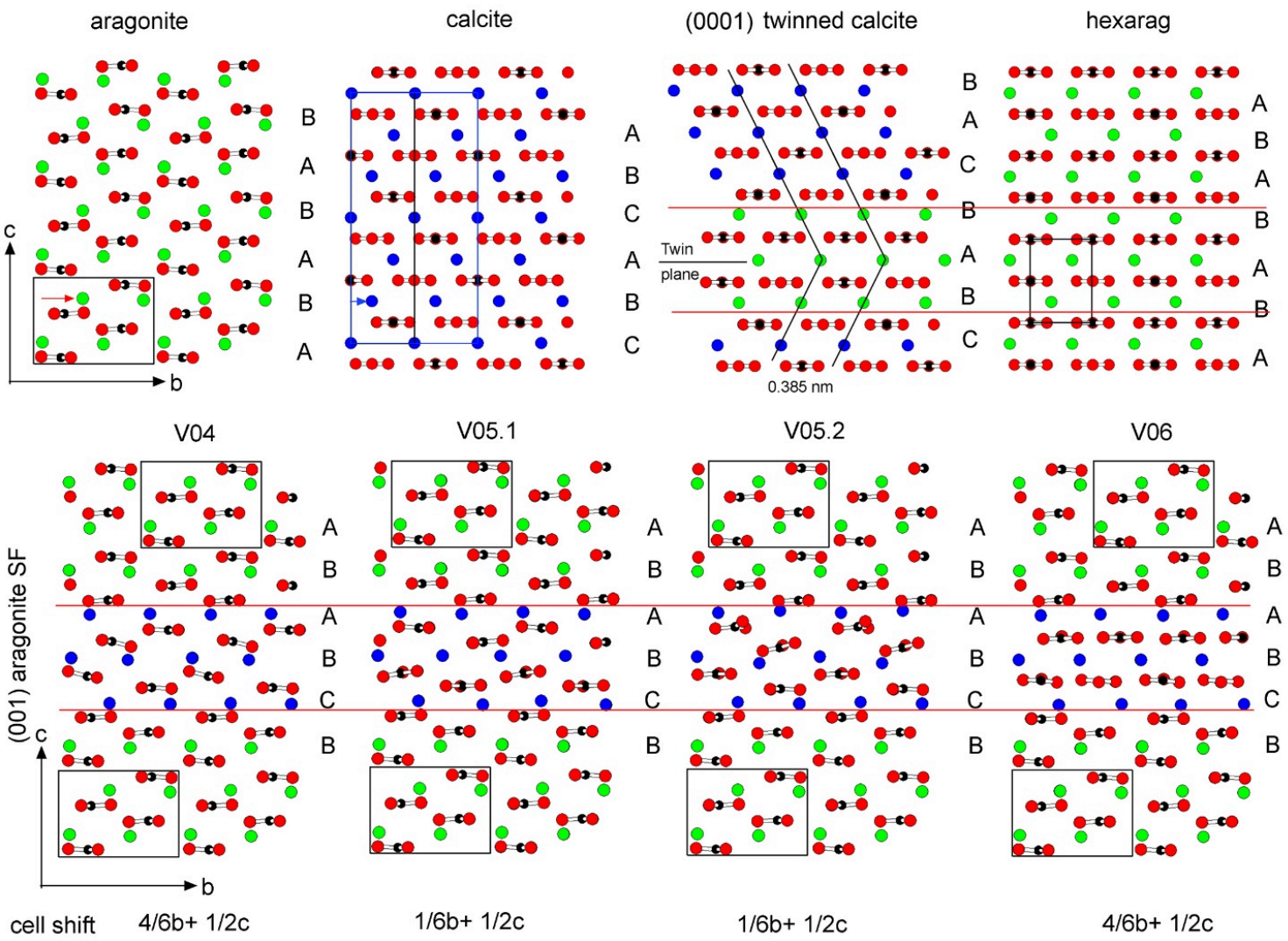


Figure 6

DFT relaxed structure models of aragonite, calcite, (0001) twinned calcite, hexarag, and the energy optimized (001) aragonite SFs types, built by insertion of various aragonite (V04, V05.1, V05.2) and calcite (V06) slabs. The starting models are shown in Fig. S8. Green and blue spheres represent Ca atoms in hexagonal and cubic stacking, respectively, while C and O atoms are shown as black and red spheres. Red and blue arrows mark 2/6y and 1/6y fractional coordinate shifts between two Ca layers in aragonite and doubled-sized calcite (blue rectangle), respectively. Black lines in (0001) twinned calcite mark spacings corresponding to 0.385 nm of the twin individuals.

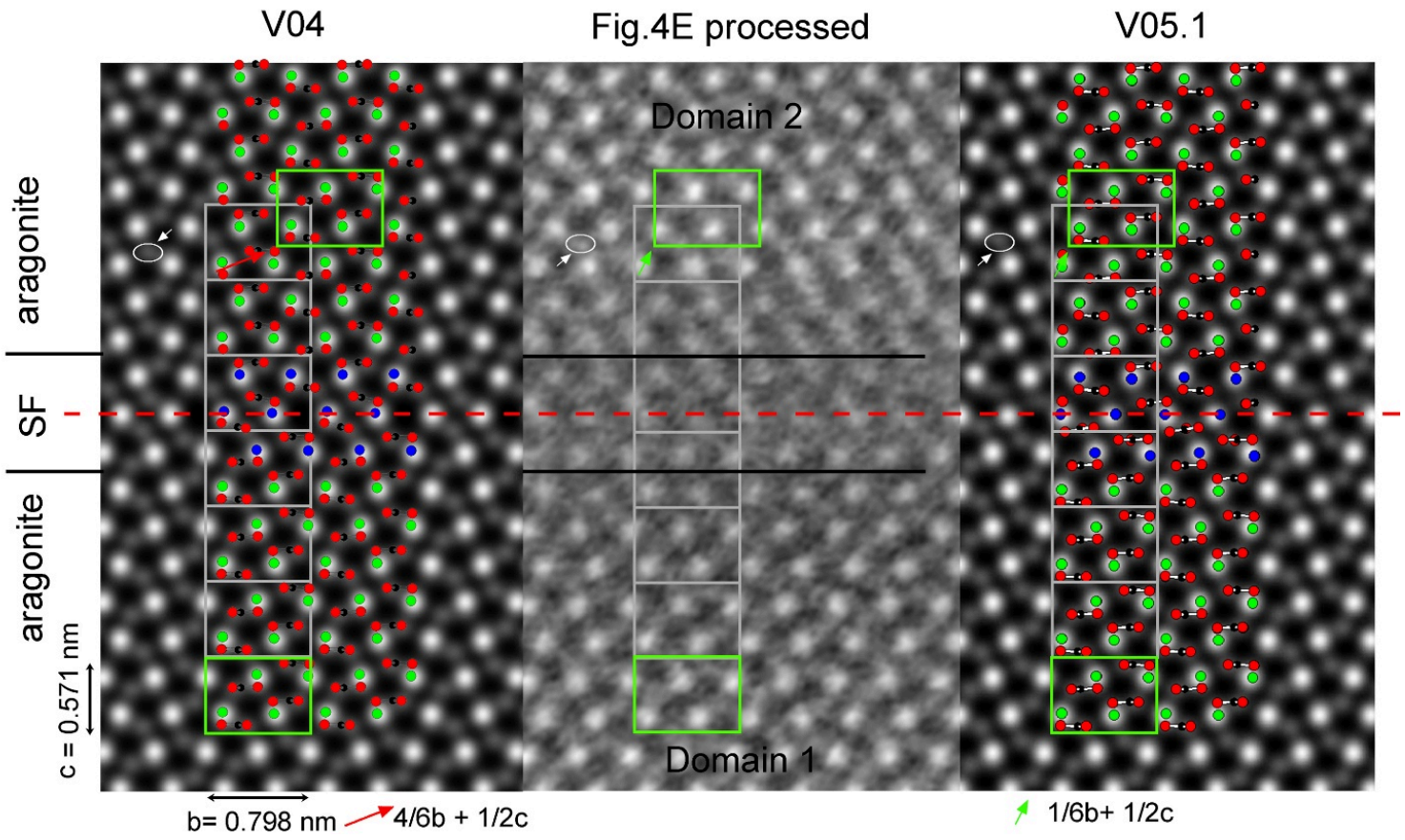


Figure 7

Simulated STEM images based on the structure models of V04 and V05.1, compared with the processed experimental image of Fig. 4E (Wiener filtered[46]). Note the pronounced shift in the positions of CO_3 groups (marked by white open ellipses) between V04 and V05.1. The shift arises from the distinct translation operations (red and green arrows) characteristic for these models. Green rectangles and a red dashed line mark the unit cell of aragonite and the boundary between domains 1 and 2, respectively.

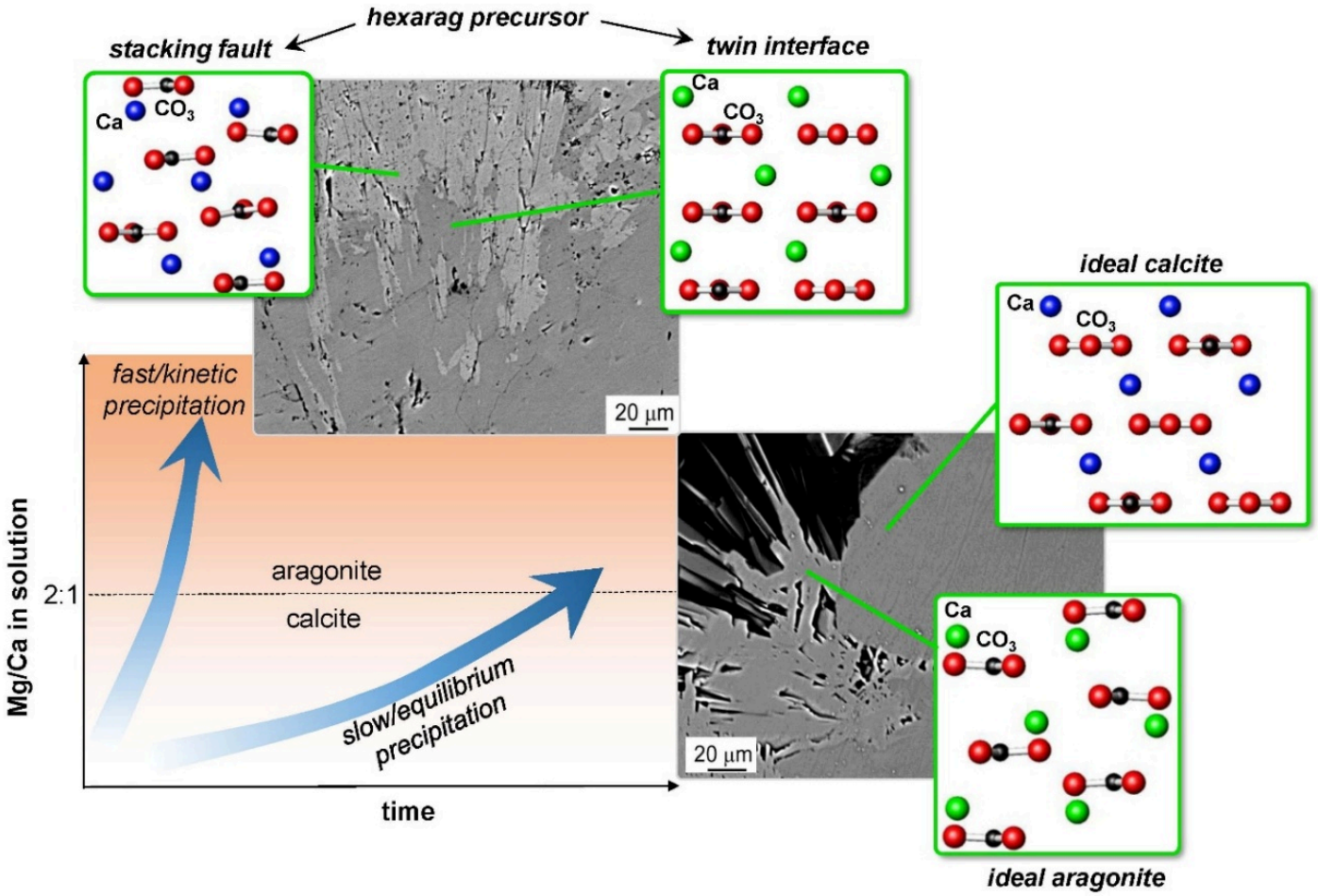


Figure 8

Conceptual model for the kinetically driven formation of transitional calcite-aragonite structures and the equilibrium-precipitated ideal carbonate structures. Under near-equilibrium growth in a stable physicochemical environment (e.g., Erzberg), the Mg/Ca = 2 threshold is reached gradually (slow/equilibrium precipitation pathway), allowing ideal aragonite to form directly on calcite. In contrast, in the non-equilibrium Berger Károly and Sonnenberg deposits, rapid increases in solution Mg/Ca ratios generate a kinetic “overshoot” (fast/kinetic precipitation pathway), promoting the formation of the hexarag precursor and its incomplete transformation products, including (001) aragonite stacking faults and (0001) calcite twins. Blue and green balls represents Ca atoms in calcitic and aragonitic stacking arrangements, respectively.

Supplementary Files

This is a list of supplementary files associated with this preprint. Click to download.

- SupplementaryInformation.pdf
- V04.cif

- V05.1.cif
- V05.2.cif
- V06.cif